Biogeosciences Discussions

First observations of global and seasonal terrestrial chlorophyll fluorescence from space

J. Joiner[1], Y. Yoshida[2], A. P. Vasilkov[2], Y. Yoshida[3], L. A. Corp[4], and
E. M. Middleton[1]

[1]NASA Goddard Space Flight Center, Greenbelt, MD, USA
[2]Science Systems and Applications, Inc., 10210 Greenbelt, Rd., Ste 400, Lanham, MD, USA
[3]National Institute for Environmental Studies (NIES), Tsukuba-City, Ibaraki, Japan
[4]Sigma Space Corp., Lanham, MD USA

Correspondence to: J. Joiner (joanna.joiner@nasa.gov)

BGD

7, 8281–8318, 2010

Measurement of regional-scale chlorophyll fluorescence

J. Joiner et al.

Abstract

Remote sensing of terrestrial vegetation fluorescence from space is of interest because it can potentially provide global coverage of the functional status of vegetation. For example, fluorescence observations may provide a means to detect vegetation stress before chlorophyll reductions take place. Although there have been many measurements of fluorescence from ground- and airborne-based instruments, there has been scant information available from satellites. In this work, we use high-spectral resolution data from the Thermal And Near-infrared Sensor for carbon Observation – Fourier Transform Spectrometer (TANSO-FTS) on the Japanese Greenhouse gases Observing SATellite (GOSAT) that is in a sun-synchronous orbit with an equator crossing time near 13:00 LT. We use filling-in of the potassium (K) I solar Fraunhofer line near 770 nm to derive chlorophyll fluorescence and related parameters such as the fluorescence quantum yield at that wavelength. We map these parameters globally for two months (July and December 2009) and show a full seasonal cycle for several different locations, including two in the Amazonia region. We also compare the derived fluorescence information with that provided by the MODIS Enhanced Vegetation Index (EVI). These comparisons show that for several areas these two indices exhibit different seasonality and/or relative intensity variations, and that changes in fluorescence frequently lead those seen in the EVI for those regions. The derived fluorescence therefore provides information that is related to, but independent of the reflectance.

1 Introduction

Vegetation is the functional interface between the Earth's terrestrial biosphere and the atmosphere. Terrestrial ecosystems absorb approximately 120 Gt of carbon annually through the physiological process of photosynthesis. About 50% of the carbon is released by ecosystem respiration processes within short time periods. The remaining carbon is referred to as Net Primary Production (NPP). Disturbances and long term

changes of ecosystems release parts of this carbon within the time frame of centuries. There are currently great uncertainties for the human impact on the magnitude of these processes.

Photosynthesis is the conversion by living organisms of light energy into chemical energy and fixation of atmospheric carbon dioxide into sugars; it is the key process mediating 90% of carbon and water fluxes in the coupled biosphere-atmosphere system. Until now, most of the information that has been acquired by remote sensing of the Earth's surface about vegetation conditions has come from reflected light in the solar domain. There is, however, one additional source of information about vegetation productivity in the optical and near-infrared wavelength range that has not been globally exploited by satellite observations. This source of information is related to the emission of fluorescence from the chlorophyll of assimilating leaves; part of the energy absorbed by chlorophyll cannot be used for carbon fixation and is thus re-emitted as fluorescence at longer wavelengths (lower energy) with respect to the absorption.

The fluorescence signal originates from the core complexes of the photosynthetic machinery where energy conversion of absorbed photosynthetically active radiation (APAR) occurs. Because the photosynthetic apparatus is an organized structure, the emission spectrum of fluorescence that originates from the photosynthetic apparatus is well known; it occurs as a convolution of broad band emission from 650 to 800 nm with two peaks in the visible and near-Infrared (NIR) at 685 and 740 nm, respectively, as shown in Fig. 1 (e.g., Meroni et al., 2009; Corp et al., 2003, 2006).

The magnitude of the emission is variable and complex. Most studies have shown that in high light conditions (i.e., in the afternoon when many visible satellite measurements are made) and when plants are under stress, fluorescence is correlated with photosynthesis (van der Tol et al., 2009). Variations in fluorescence and photosynthesis in the afternoon occur when protective mechanisms intervene to prevent damage by harmful radicals that are formed under these conditions. Therefore, remotely-sensed chlorophyll fluorescence provides a means to estimate global instantaneous vegetation carbon-related processes that are of major interest for precision farming, forest

management, and assessment of the terrestrial carbon budget (e.g., Campbell et al., 2008).

To date, space-based approaches to provide insight into plant physiological status have relied primarily on the measured reflectance that provides information about chlorophyll content. There is observational evidence that chlorophyll fluorescence supplies information content independent of reflectance-based spectral vegetation indices (e.g., Meroni and Colombo, 2006; Guanter et al., 2007; Meroni et al., 2008; Middleton et al., 2008, 2009). A measurement of chlorophyll fluorescence provides an important direct approach for diagnosing vegetation stress, associated with reduced photosynthetic functionality, before chlorophyll reduction occurs. It has therefore been a goal of satellite missions proposed to the European Space Agency (ESA) and the United States National Aeronautics and Space Administration (NASA) (e.g., Davidson et al., 2003).

The measurement of solar-induced chlorophyll fluorescence, F, from space is challenging, because its signal (typically 1–5% in the near-IR) must be differentiated from the much larger reflectance effect. F has been detected from ground- and airborne-based instrumentation by exploiting the fact that F is a proportionally larger fraction of the total radiance within dark lines and bands of the atmospheric spectrum (e.g., Moya et al., 2004; Zarco-Tejada et al., 2009). These dark features include both very narrow solar Fraunhofer lines and wider telluric absorption features such as the O_2-B band at 687 nm and the O_2-A band near 760 nm.

The O_2 absorption features, primarily the O_2-A band, have been used more extensively with recent ground-, aircraft-, and space-based spectrometers that have spectral resolutions of tenths of a nanometer and larger (individual lines not resolved), because these bands appear wider and deeper and align more closely with the peaks of F (see e.g., the review by Meroni et al., 2009, and more than 40 references within).

Air- and space-based remote sensing of F by utilization of the O_2 bands is complicated, because F must be disentangled from the reflectance signal. On the ground, this is typically achieved by making a separate measurement of the incident solar

irradiance. In air- and space-borne applications, one must additionally account for absorption and scattering that takes place between the ground and instrument that further dilutes the F signal (e.g., Guanter et al., 2010).

Using an aircraft instrument with high spatial resolution, a measurement in a non-fluorescing pixel can be used to perform this atmospheric correction (e.g., Maier et al., 2002, 2003). Rascher et al. (2009) mapped the relative distribution of fluorescence at 760 nm using a spectrometer mounted on an aircraft. They used an empirical normalization approach to correct for problems with radiometric calibration. In their approach, observations over bare soil at identical illumination conditions were used as a reference.

The only space-based detection of F to date was achieved by Guanter et al. (2007) with the MEdium Resolution Imaging Spectrometer (MERIS) (Rast et al., 1999) aboard the European Space Agency's (ESA's) ENVIronmental SATellite (ENVISAT). MERIS has two channels near the O_2-A band, one near the peak absorption at 760.6 nm with a 3.75 nm bandwidth, and one used as a reference band in the nearby continuum at 753.8 nm. MERIS makes measurements at a moderate spatial scale for land studies (better than 300 m per pixel in its Full Resolution mode).

The MERIS fluorescence retrieval was made for a limited area on one day. A radiative transfer model and other derived properties were used to correct for atmospheric effects and solve for the reflectance ρ and F. The derived F was compared with the other MERIS-derived biophysical products.

Here, instead of using O_2-A band absorption, we make use of unique high spectral resolution measurements from the Japanese Greenhouse gases Observing SATellite (GOSAT). With GOSAT, we observe filling-in of the potassium (K) I solar Fraunhofer line near 770 nm. Though not designed for this purpose, we demonstrate that fluorescence can be conclusively and directly measured from space and that GOSAT may be used to retrieve F at a regional scale.

The paper is organized as follows: Sect. 2 describes the GOSAT satellite observations used here. The simulated effect of fluorescence on GOSAT observations and its

Full Screen / Esc

Printer-friendly Version

Interactive Discussion

dependence on surface albedo are shown in Sect. 3. Our approach for the retrieval of the chlorophyll fluorescence signal is given in Sects. 4–5. We show averaged monthly results for July and December 2009 in Sect. 6 along with full seasonal cycles for several regions. We also compare our fluorescence retrievals with the MODIS enhanced vegetation index (EVI). Conclusions are given in Sect. 7.

2 GOSAT observations

GOSAT is a satellite mission that was designed to monitor the global distribution of the greenhouse gases CO_2 and CH_4 (Yokota et al., 2009). It was jointly developed by the Japanese Ministry of the Environment (MOE), the National Institute for Environmental Studies (NIES), and the Japanese Aerospace Exploration Agency (JAXA). GOSAT was launched on 23 January 2009 into a sun-synchronous orbit with a descending node equatorial crossing time near 13:00 LT. Its mean altitude is 666 km, and it has a 3 day repeat cycle.

Here we use spectra from the GOSAT Thermal And Near-infrared Sensor for carbon Observation-Fourier Transform Spectrometer (TANSO-FTS) (Kuze et al., 2009). The TANSO-FTS measures backscattered solar radiation in three shortwave infrared (SWIR) regions, referred to as "bands", centered at 0.76, 1.6, and 2.0 µm. It has a nadir ground footprint of 10.5 km diameter.

GOSAT also has a Cloud and Aerosol Imager (CAI) with four bands at 0.38, 0.67, 0.87, and 1.6 µm with footprints between 0.5 and 1.5 km. The CAI was designed to be used for detection and correction of cloud and aerosol effects in the TANSO-FTS spectra.

Chlorophyll fluorescence can be measured primarily within band 1 that extends from approximately 758 to 775 nm and encompasses the O_2-A band. The primary function of the O_2-A band for GOSAT is to account for the effects of cloud and aerosol within the CO_2 and CH_4 bands. In band 1, the TANSO FTS has a full-width half maximum (FWHM) of the unapodized Instrument Line-Shape Function (ILSF) between 0.367 and

Measurement of regional-scale chlorophyll fluorescence

J. Joiner et al.

Measurement of regional-scale chlorophyll fluorescence

J. Joiner et al.

0.356 cm^{-1} (or approximately 0.022 nm), or a corresponding resolving power ($\nu/\Delta\nu$) of > 35000. Figure 2 shows the ILSF and spectral sampling within its FWHM. For a typical scene radiance (Lambertian surface albedo of 0.3 at 30° solar zenith angle), the signal-to-noise ratio (SNR) is > 300.

3 Simulated effect of fluorescence on GOSAT measurements

Here, we simulate the effect of fluorescence on GOSAT observations in the vicinity of the K I line near 770 nm. We use the so-called KPNO2010 high spectral resolution solar irradiance reference spectrum (Chance and Kurucz, 2010), line parameters from the HITRAN 2004 database (Rothman et al., 2005), and a line-by-line code provided by R. Spurr (personal communication, 2010). Because Rayleigh optical thickness is low at these wavelengths, we did not include atmospheric scattering in these simulations. Calculations were performed on a grid with spacing 0.01 cm^{-1} or 6e-4 nm. The solar spectrum was interpolated onto that grid.

Figure 3 shows simulated monochromatic and GOSAT reflectance spectra computed for a spectrally constant fluorescence of 3 mW/m^2/sr/nm, solar zenith angle of 45°, and a surface albedo of 0.2. The filling-in of the K I line near 770.1 nm is shown along with several O$_2$ absorption lines including two weak lines on either side of the K I filling-in feature.

Figure 4 shows the dependence of the simulated filling-in of both the K I line and the 769.9 nm O$_2$ line on the surface albedo for two values of fluorescence. The K I line provides signficantly more filling-in than that of the O$_2$ line. The surface albedo has little effect on the O$_2$ line depth, but does affect the observed filling-in, particularly of the K I line. The O$_2$ line depth depends on the satellite viewing geometry and surface pressure (not shown). The filling-in does not depend upon these parameters within the K I line, as there is no significant terrestrial absorption within this dark solar line.

4 Approach

Figure 5 shows both observed (normalized) solar irradiance and sample Earth-view radiance spectra from the TANSO-FTS band 1 and a zoom in at the wavelengths used here for fluorescence retrieval (bottom panel). Resolved lines within the O_2-A band are apparent in the Earth spectrum. Solar Fraunhofer lines are seen in both the solar and Earth spectra. Note that there may be small errors in absolute wavelength calibration and that the asymmetric ILSF also produces an apparent wavelength shift between observations and exact positions of solar Fraunhofer lines. There may also be errors in the absolute radiometric calibration as the instrument radiometric sensitivity has decreased by about 10% from pre-flight values in band 1 and vicarious calibration is required for correction.

The potassium (K) I line is one of the deepest solar Fraunhofer lines within GOSAT's band 1 ($\sim$755–775 nm). Although there are several other Fraunhofer lines lying closer to the peak of the 740 nm fluorescence peak, the K I line was found to be the most ideal to observe chlorophyll fluorescence owing to its greater line depth and lack of terrestrial oxygen absorption. The K I line falls between several weak O_2 lines and can be observed in relative isolation with GOSAT's high spectral resolution.

The use of the K I line substantially simplifies a retrieval of F as compared with the O_2-A band; atmospheric correction is not necessary as the absorption near it is negligible. The detection of F using this method was thought to be unfeasible owing to the high vegetation reflectance in the near-IR known as the red edge. However, at GOSAT's high spectral resolution and SNR, and due to its large footprint that ensures capture of substantial photon emissions, our simulations indicate that detection of ecosystem-scale chlorophyll fluorescence can be achieved.

We jointly retrieve the surface reflectivity ρ (assumed Lambertian surface) and the additive chlorophyll fluorescence signal F as a function of wavelength λ over the narrow (0.35 nm) spectral band 769.90–770.25 nm using the following model for the observed

Earth spectral radiance $I(\lambda)$:

$$I(\lambda) = \rho E(\lambda)/\pi + F + \frac{\partial I(\lambda)}{\partial \Delta\lambda}\Delta\lambda, \tag{1}$$

where $E(\lambda)$ is the solar irradiance and $\Delta\lambda$ is the wavelength shift between Earth and solar spectra. Here, several GOSAT solar spectra taken closest in time to Earth radi-
5 ance observations (within a few hours) are averaged together to produce a composite spectrum. Before using Eq. (1), we first perform a rough adjustment to spectrally align the solar and Earth spectra. We then add the wavelength shift term in Eq. (1) to the fit to further improve the alignment.

Here, we assume a constant wavelength dependence of F and ρ over this band.
10 This assumption could be relaxed as would be appropriate for a larger spectral fitting window as discussed by e.g., Meroni et al. (2010). We could also account for scattering and absorption using a radiative transfer code. Note that the spectral dependence of atmospheric scattering is practically constant over this narrow window, so the neglect of it should have an insignificant effect on the retrieval of fluorescence. Similarly, a
15 constant calibration offset in the solar irradiance will not affect the derived fluorescence as the error will be absorbed in the retrieved value of ρ. An error in absolute calibration of $I(\lambda)$, however, will be present in the retrieved F.

The filling-in effect of rotational-Raman scattering at these wavelengths should be small as compared with the F signal (Sioris et al., 2003) at most observed solar zenith
20 angles. Indeed, we found no evidence of a significant filling-in effect due to rotational-Raman scattering except at the highest solar zenith angles (SZA) when low PAR levels likely limit photosynthesis. These high SZA data were therefore eliminated from data shown here.

We use a standard weighted least squares fitting to derive ρ and F. There are
25 two weak O_2 lines located within the window, as shown by the red portions of the reflectance spectra in Fig. 6. We effectively remove these wavelengths (769.96–770.02 and 770.09–770.13 nm) from the fit by assigning large errors or no weight to them. All other wavelengths are weighted equally.

Our initial results showed positive values of fluorescence over the Sahara where none was expected. The root cause was found to be unexplained systematic spectral structure in the core of the K I line. An example is shown in the right panel of Fig. 6 for an observation taken over the Sahara. This spectral structure was initially fit by our algorithm as a small positive filling-in. We therefore found it necessary to adjust the algorithm in order to account for this spectral structure. To accomplish this, we derived an average spectral signature of pixels where we expect zero fluorescence. Here we used clear-sky pixels from one day over the Sahara. We checked other days and obtained a similar result. We then added a term to account for this spectral structure, i.e.,

$$I(\lambda) = \frac{\rho E(\lambda)}{\pi} + F + \frac{\partial I(\lambda)}{\partial \Delta \lambda} \Delta \lambda + AH(\lambda), \tag{2}$$

where $H(\lambda)$ is the derived mean radiance residual and A is the coefficient of the fit. This reduced the fluorescence bias over the Sahara and improved the fits to the radiance spectra globally.

We found that adding additional terms involving a polynomial in wavelength expansion of $H(\lambda)$ provided a further improvement to the radiance fit and reduced the standard deviation of the radiance residuals, i.e.,

$$I(\lambda) = \frac{\rho E(\lambda)}{\pi} + F + \frac{\partial I(\lambda)}{\partial \Delta \lambda} \Delta \lambda + AH(\lambda) + BH(\lambda)(\lambda - \lambda_0) + CH(\lambda)(\lambda - \lambda_0)^2, \tag{3}$$

where B and C are additional coefficients, and λ_0 is the wavelength in the center of our fitting window. With this treatment applied globally, the positive bias in fluorescence over the Sahara was eliminated, though a small negative bias in fluorescence remains there and elsewhere, particularly where fluorescence is near the detection limit. The largest adjustments to F using these terms are over the Sahara (on average $\sim$2–3 mW/m^2/sr/nm) while adjustments elsewhere are smaller ($\sim$1 mW/m^2/sr/nm over inactive regions and 1.2–2 mW/m^2/sr/nm over active vegetation). The majority of the correction results from the use of the A coefficient, but second order effects result from application of the B and C coefficients.

Examples of the fitted residual spectral structure are shown in Fig. 7 (dotted lines) for pixels over active vegetation in the Eastern United States (left) and Sahara (right). The fitted filling-in structure due to fluorescence ($F/\rho E(\lambda)$ in %) is also shown in Fig. 7. Samples of the overall fits to normalized reflectance spectra for the same pixels are shown in Fig. 6 along with the fit residuals (observed minus fitted, %). For the wavelengths used in the fits, the residuals are generally within about ± 0.5%.

5 Further GOSAT data processing for F retrievals

We first removed cloudy data by two different methods. The remaining data were averaged in 2 degree latitude × 2 degree longitude grid boxes. In the first cloud filtering method, the concept of the cloud radiance fraction (CRF) is used. CRF is defined as the fraction of pixel radiance coming from clouds. The CRF is a useful quantity for cloudy pixel screening because there can be situations of high cloud fractions with nearly transparent clouds that would minimally affect our retrievals, while there could also be cases of low cloud fractions but extremely bright clouds that we would not want to include in our sample. Here, we used CRF derived at 450 nm with the Ozone Monitoring Instrument (OMI) (Levelt et al., 2006) that flies on the Aura spacecraft. The CRF is supplied in the standard NO_2 data product (Bucsela et al., 2006). OMI observations are made over the same geographical area within $\sim$< 2 h of GOSAT. We used only pixels with a cloud radiance fraction <10%.

In the second cloud filtering method, we used the cloud fraction from the GOSAT CAI. Here, we removed pixels with estimated cloud fractions >10%. This provided results similar to those with the CRF. All results shown here use the second method.

We also examined radiance residuals in order to quality control the retrievals. We tested several different thresholds on the residuals including a checks on the maximum residual and mean (over wavelength) residual. We found that some pixels exhibited more noise than others. However, removing pixels with higher-than-average noise did not significantly alter the results and in some cases significantly decreased the number

of samples per gridbox, leaving many gridboxes with no samples. Therefore, in the results shown below, we did not remove any pixels based on high radiance residuals.

The number of pixels averaged for a particular gridbox in a month varied from 1 to 39, with most grid boxes having between 2 and 12 observations. In dry areas with less clouds, like northern Africa, Saudi Arabia and central Australia, the number of observations ranges from about 16–28 on average.

Figure 8 shows the retrieved monthly mean F for July 2009 in the same units as the Earth radiance. Another useful quantity that can be derived is the normalized instantaneous fluorescence quantum yield, Φ, given by

$$\Phi = F_f/\text{APAR} = F_f/(\text{FPAR} \times \text{PAR}), \tag{4}$$

(e.g., Louis et al., 2005), where F_f is the fluorescence flux, FPAR is the fraction of radiation intercepted by the canopy, and PAR is the instantaneous (clear sky) broadband photosynthetically active radiation (400–700 nm). Here, we use FPAR derived from the MODerate-resolution Imaging Spectroradiometer (MODIS) (Myneni et al., 2002) as shown in Fig. 9. We estimated clean-sky PAR (no clouds or aerosol) using the radiative transfer code of Fu and Liou (1992) and monthly mean total column ozone from OMI with ozone profile information from the GEOS-5 Data Assimilation System (Rienecker et al., 2007). We also used water vapor profiles from GEOS-5. Assuming that our derived fluorescence signal is isotropic, which is the traditional expectation, we may now estimate Φ for the narrow wavelength band (~1 nm) considered here such that Φ is unitless. Fig. 10 shows $\Phi(770\,\text{nm})$ for July 2009. As FPAR becomes small, any errors in the F, FPAR, or PAR become amplified. Therefore, we only show Φ for FPAR> 0.3.

As the derived Φ is somewhat noisy owing to the inclusion of incomplete information from other sensors, most subsequent results will be shown as F divided by cosine of the solar zenith angle (SZA), a proxy for PAR. We will refer to this as "scaled fluorescence". The scaling accounts for the solar zenith angle dependence of the incoming solar irradiance, but does not account for spatial or temporal variations in FPAR, such as those related to the leaf area index (LAI). If the fluorescence is assumed isotropic,

we may consider scaled F, like Φ, to be a unitless quantity. Note that this scaling amplifies the retrieved small negative values of fluorescence that occur when we are near the detection limit; These negative values are prevalent at high solar zenith angles in the winter hemispheres when vegetation is inactive.

6 Results

Figure 11 shows monthly mean scaled F for July and December 2009 as retrieved from the K I solar line. The expected seasonal variation is definitively shown, namely, higher Northern Hemisphere terrestrial activity in July versus higher activity in the Southern Hemisphere in December. We also show the analogous data for the Enhanced Vegetation Index (EVI) (Huete et al., 2002), a widely utilized vegetation reflectance-based index to indicate relative greenness and to infer photosynthetic function, which was obtained over the same time periods from NASA's Aqua MODIS sensor (Fig. 12). The Aqua satellite has an ascending node equator crossing near 13:30 LT, similar to that of GOSAT.

We compare and contrast the monthly averages for the derived and scaled F with those for EVI, for the eight geographic regions outlined in Fig. 12. Although there are similarities between the scaled F and EVI values, some obvious differences are also evident. All of these plots show a large amount of scatter in the relationship between scaled F and EVI. Details of these differences are seen in the scatter diagrams of Figs. 13–15.

These continental or large regional blocks obviously include a variety of vegetation types such as forests, grasslands, and croplands that have different F and EVI values. Even though the plots show significant scatter, for most regions there is an evident positive but non-linear relationship between F and EVI, but with a great deal of scatter. These trends are similar in shape and intensity value ranges in July in the Northern Hemisphere (Fig. 13, panels 1, 2, 3, 4). In contrast, these same North American regions exhibit very low F (<2) across a range of EVI values in December (Fig. 14), indicating low photosynthetic by standing green vegetation (e.g., coniferous forests).

Another example is that some regions display moderate EVI values (0.2–0.4) that imply the presence of green vegetation but where the fluorescence is at or near the detection threshold. This is particularly apparent in the July panel (Fig. 13, panel 5) for South America, which may indicate that the vegetation has retained greenness but is not physiologically active during the dry season.

Africa shows the most exciting example, with a clear positive and linear relationship for F:EVI across the observed greater range of F and EVI values in both July and December (Figs. 13 and 14.) This occurs because Africa spans both the northern and southern hemispheres and includes the full range of vegetation types, including the extremes of tropical forests and the Sahara desert. Indonesia, a tropical low latitude region, shows no correlation between EVI and fluorescence and has the same F:EVI cluster in both the July and December seasons.

Southern Hemisphere regions (Fig. 14) during the growing season (December) exhibit highly variable F versus EVI, with no clear relationships demonstrated here. South America and Australia show very low F in July (winter) over most of the EVI range (<0.4).

Australia has mostly low to moderate EVI values during these months that show no correlation with fluorescence. The maps in Fig. 11 indicate that active fluorescence occurs over Australia primarily along the continental edges in the austral spring/early summer, a pattern not expressed distinctly in the corresponding EVI map.

Scatter diagrams using the scaled F are qualitatively similar to those using Φ (Fig. 15), and have the advantage of reliance only on the GOSAT data. Moreover, the diagrams that use Φ show more variability and less correlation with EVI, most probably due to increased errors that result from inclusion of the MODIS FPAR satellite product. This further supports our use of the scaled F to demonstrate the capability of the GOSAT sensor to measure chlorophyll fluorescence over land areas.

Figure 16 shows the full seasonal cycle in scaled F and EVI for a few selected regions. As expected, over the Eastern US, a clear increase in scaled F is seen during the spring months (April and May) with a peak in early summer (June/July).

This seasonal cycle is also seen in the EVI which indicates a greater seasonal contrast (maximum vs. minimum) than the scaled F.

We next examine two Amazonia regions, one near the East coast of Brazil and one more towards the west in the central Amazon rainforest region (Fig. 16, panels 2–3). In the westernmost Amazon pixel (Fig. 16, panel 2), the dry season (July–November) green up reported by Huete et al. (2006) for 2005 is seen here between September 2009 and January 2010 in both scaled F and EVI, with scaled F leading by approximately one month beginning in August. In this region, trees with deep roots may have more continuous access to deep soil moisture (e.g., Nepstad et al., 1994). Here, EVI follows PAR which depends primarily on cloud cover and peaks during the dry season (Huete et al., 2006). However, this temporal pattern is not captured in the MODIS Normalized Difference Vegetation Index (NDVI) (not shown); NDVI values typically peak in June/July for this region and decline to a minimum in December. In the other regions shown here, the NDVI is qualitatively similar (in the seasonal cycle) to the EVI.

In the eastern Amazon area (Fig. 16, panel 3), a different pattern is seen with a brown-down in the early part of the dry season in both EVI and scaled F, consistent with analysis over grassland pasture sites in previous years by Huete et al. (2006). In this region, forest conversion has occurred where deep-rooted trees have been replaced with shallow-rooted vegetation that responds more to soil moisture stress. The steepest decline in scaled F occurs from April to May, while a sharp decline in EVI is seen from June through September. The scaled F shows an increase starting in September, while the EVI increase begins in October.

Over Indonesia (Fig. 16, panel 6), there is little seasonal change in EVI, although scaled F shows a significant minimum in June during the dry season when biomass burning typically takes place. El Niño began around this time in 2009 leading to a drier than normal season; widespread haze due to fires was observed in the region from June through September. Logging and forest conversion have occurred here, resulting in more vegetation stress during the dry season, especially during dry years associated with El Niño.

Title Page

Abstract | Introduction

Conclusions | References

Tables | Figures

◀ | ▶|

◀ | ▶

Back | Close

Full Screen / Esc

Printer-friendly Version

Interactive Discussion

In the north of Australia (Fig. 16, panel 7), EVI (and NDVI) generally peaks in the austral autumn owing to the summer monsoonal rains. In contrast, we see a more broad peak in F starting earlier. Higher spatial scale studies show significant variability in NDVI in this region as well as interannual variability (e.g. Martin et al., 2009). A different pattern is seen in the EVI in the south western region of Australia with a distinct peak in the spring (Fig. 16, panel 9). This pattern is not seen in the derived fluorescence. These regions warrant further study and investigation into potential effects of sub-pixel variability and sources of error in the satellite-derived products.

7 Conclusions and ongoing work

While satellite-derived vegetation indices such as the EVI provide estimates of the potential (or maximum) photosynthesis, the fluorescence retrievals shown here are the first regional-scale measures of actual (as compared with inferred potential) instantaneous and dynamic photosynthetic activity derived by measuring light emission that originates from the cores of the photosynthetic machinery. Therefore, we do not necessarily expect to see a strong correlation between fluorescence and EVI. In fact, our results indicate that our derived fluorescence is indeed providing information that is independent of EVI, and could be used to supplement it to provide important global productivity seasonal dynamics information. We intend to pursue this possibility further.

We have demonstrated that space-based missions that were specifically designed to measure CO_2 concentrations can also be used to measure an important value-added carbon product: regional-scale chlorophyll fluorescence. Further development of this product and studies using this data will help to maximize the benefits of space-based carbon missions such as GOSAT and a reflight of the NASA Orbiting Carbon Observatory (OCO) (Crisp et al., 2004).

The FLourescence EXplorer (FLEX) mission (Rascher, 2007; European Space Agency, 2008) was selected in 2006 for assessment as the result of the European Space Agency's call for core Earth Explorer Mission ideas and has been since re-proposed. Our study provides evidence that such a mission could provide important information on photosynthetic efficiency of terrestrial ecosystems at a global scale. This information combined with data from other satellites will help to better quantify relationships between the carbon and water cycles and their coupling with the Earth's climate. The FLEX missions plans to utilize the O_2-A band for chlorophyll fluorescence retrievals (Guanter et al., 2010), whereas OCO-2 could use the solar K Fraunhofer line since its spectral coverage and resolution is similar to GOSAT's.

A chlorophyll fluorescence product may also be feasible from Geostationary (GEO) orbit using instrumentation being proposed for the NASA decadal survey GEO-Coastal and Air Pollution Events (GEO-CAPE) mission. This would provide important information regarding the links between pollutants, such as tropospheric O_3 that can damage vegetation, and climate, through the uptake of CO_2, the primary anthropogenic greenhouse gas.

As most previous studies of F have been conducted at the leaf scale and at near-surface, care must be taken to properly interpret this large pixel data. The influence of canopy structure needs to be investigated in order to fully understand its influence on retrieved fluorescence and consequently derived relationships with key carbon-related parameters such as gross primary production (GPP) and light-use efficiency (LUE) (Damm et al., 2010).

We have reported fluorescence in appropriate units, and our values fall within the low end of ranges of other measurements reported in Meroni et al. (2009). We have not taken into account the directionality of the emitted fluorescence, although this is a reasonable approach since F has traditionally been assumed to be isotropic. There may also be errors in absolute calibration of the Earth radiance data and errors associated with our spectral fitting. Therefore, our reported absolute values must be interpreted with caution. The association of F with biomes, rather than whole continents or arbitary

large regions, will improve the understanding of this signal.

We are currently processing more GOSAT data in an effort to map global complete seasonal cycles and to quantify interannual variations in fluorescence owing to events such as extreme drought. We have also begun to examine our derived fluorescence in conjunction with satellite precipitation data.

Accounting for chlorophyll fluorescence in the K I line could assist in the interpretations made for F in the O_2-A band. Furthermore, this should also help to improve the retrieval of CO_2, as well as aerosol and cloud information from the O_2-A band. This band was designed to be an integral part of both the GOSAT and NASA OCO missions (e.g., Kuang et al., 2002; Crisp et al., 2004). It has been used with the SCanning Imaging Absorption SpectroMeter for Atmospheric CHartographY (SCIAMACHY) to obtain an accurate description of the solar light path over both clear and cloudy pixels (Reuter et al., 2010) to aid in CO_2 retrievals. Without proper accounting for the variability of the fluorescence signal, the accuracy of CO_2, cloud, and aerosol information from these sensors will be degraded.

References

Bucsela, E. J., Celarier, E. A., Wenig, M. O., Gleason, J. F., Veefkind, J. P., Boersma, K. F., and Brinksma, E. J.: Algorithm for NO_2 vertical column retrieval from the Ozone Monitoring Instrument, IEEE Trans. Geosci. Remote Sens., 44, 1245–1258, 2006. 8291

Campbell, E., Middleton, E. M., Corp, L. A., and Kim, M. S.: Contribution of chlorophyll fluorescence to the apparent vegetation reflectance, Sci. Total Environ., 404, 433–439, 2008. 8284

Chance, K. and Kurucz, R. L.: An improved high-resolution solar reference spectrum for Earth's atmosphere measurements in the ultraviolet, visible, and near infrared, J. Quant. Spectrosc. Radiat. Trans., 111, 1289–1295, 2010. 8287

Corp, L.A., McMurtrey, J. E., Middleton, E. M., Mulchi, C. L., Chappelle, E. W., and Daughtry, C. S. T.: Fluorescence Sensing Systems: In vivo detection of biophysical variations in field corn due to nitrogen supply, Remote Sens. Environ., 86, 470–479, 2003. 8283

Measurement of regional-scale chlorophyll fluorescence

J. Joiner et al.

Corp, L. A., Middleton, E. M., McMurtrey, J. E., Campbell, P. K. E., and Butcher, L. M.: Fluorescence sensing techniques for vegetation assessment, Appl. Opt., 45, 1023–1033, 2006. 8283

Crisp, D.: The Orbiting Carbon Observatory (OCO) mission, Adv. in Space Res., 34, 700–709, 2004. 8296, 8298

Damm, A., Elbers, J., Erler, A., et al.: Remote sensing of sun-induced fluorescence to improve modeling of diurnal courses of gross primary production (GPP), Global Change Biology, 16, 171–186, doi:10.1111/j.1365-2486.200901908.x, 2010. 8297

Davidson, M., Berger, M., Moya, I., Moreno, J., Laurila, T., Stoll, M.-P., and Miller, J.: Mapping photosynthesis from space – a new vegetation-fluorescence technique, ESA Bull., 116, 34–37, 2003. 8284

European Space Agency:. ESA SP-1313/4 Candidate Earth Explorer Core Missions - Reports for Assessment: FLEX – FLuorescence EXplorer, published by ESA Communication Production Office, Noordwijk, The Netherlands, http://esamultimedia.esa.int/docs/SP1313-4_FLEX.pdf., 2008. 8297

Fu, Q. and Liou, K.-N.: On the correlated k-distribution method for radiative transfer in nonhomogeneous atmospheres, J. Atmos. Sci., 49, 2139–2156, 1992. 8292

Guanter, L., Alonso, L., Gómez-Chova, L., Amorós-López, J., Vila-Francés, J., and Moreno, J.: Estimation of solar-induced vegetation fluorescence from space measurements, Geophys. Res. Lett., doi:10.1029/2007GL029289, 2007. 8284, 8285

Guanter, L., Alonso, L., Gómez-Chova, Meroni, M., Preusker, R., Fischer, J., and Moreno, J.: Developments for vegetation fluorescence retrieval from spaceborne high-resolution spectrometry in the O_2-A and O_2-B absorption bands, J. Geophys. Res., 115, D19303, doi:10.1029/2009JD013716, 2010. 8285, 8297

Huete, A. R., Didan, K., Miura, T., Rodriguez, E. P., Gao, X., Ferreira, L. G.: Overview of the radiometric and biophysical performance of the MODIS vegetation indices, Remote Sens, Environ,, 83, 195–213, 2002. 8293

Huete, A. R., Didan, K., Shimabukuro, Y. E., Ratana, P., and Saleska, S. R.: Amazon rainforests green-up with sunlight in dry season, Geophys. Res. Lett., 33, L06405, doi:10.1029/2005GL025583, 2006. 8295

Kuang, Z., Margolis, J., Toon, G., Crisp, D., and Yung, Y.: Spaceborne measurements of atmospheric CO_2 by high-resolution NIR spectrometry of reflected sunlight: an introductory study, Geophys. Res. Lett., 29, 1716, doi:10.1029/2001GL014298, 2002. 8298

Title Page

Abstract | Introduction

Conclusions | References

Tables | Figures

|◄ | ►|

◄ | ►

Back | Close

Full Screen / Esc

Printer-friendly Version

Interactive Discussion

Kuze, A., Suto, H., Nakajima, M., and Hamazaki, T.: Thermal and near infrared sensor for carbon observation Fourier-transform spectrometer on the Greenhouse Gases Observing Satellite for greenhouse gases monitoring, Appl. Opt., 48, 6716–6733, 2009. 8286

Levelt, P. F., van den Oord, G. H. J., Dobber, M. R., et al.: The Ozone Monitoring Instrument, IEEE Trans. Geosci. Rem. Sens., 44, 1093–1101, 2006. 8291

Louis, J., Ounis, A., Ducruet, J.-M., Evain, S., Laurila, T., Thum, T., Aurela, M., Wingsle, G., Alonso, L., Pedros, R., and Moya, I.: Remote sensing of sunlight-induced chlorophyll fluorescence and reflectance of Scots pine in the boreal forest during spring recovery, Remote Sens. Environ., 96, 37–48, 2005. 8292

Maier, S. W., Günther, K. P., and Stellmes, M.: Remote sensing and modelling of solar induced fluorescence, Proc. 1st Workshop Rem. Sens. Solar Induced Vegetation Fluorescence, ES-TEC, Noordwijk, The Netherlands, 19–20 June, 2002. 8285

Maier, S. W., Günther, K. P., and Stellmes, M.: Sun-induced fluorescence: A new tool for precision farming, in: Digital imaging and spectral techniques: Applications to precision agriculture and crop physiology, 209–222, edited by: VanToai, T., Major, D., McDonald, M., Schepers, J., and Tarpley, L., Madison, American Society of Agronomy, 2003. 8285

Martin, D., Grant, I., Jones, S., and Anderson, S.: Development of satellite vegetation indices to assess grassland curing across Australia and New Zealand, in: Innovations in Remote Sensing ad Photogrammetry, Lecture Notes in Geoinformation and Cartography, Part 3, edited by: Cartwright, W., Gartner, G., Meng, L., et al., Springer Berlin Heidelberg, doi:10.1007/978-3-540-93962-7_17, 211–227, 2009. 8296

Meroni, M. and Colombo, R.: Leaf level detection of solar induced chlorophyll fluorescence by means of a subnanometer resolution spectroradiometer, Remote Sens. Environ., 103, 438–448, 2006. 8284

Meroni, M., Picchi, V., Rossini, M., Cogliati, S., Panigada, C., Nali, C., Lorenzini, G., Colombo, R.: Leaf level early assessment of ozone injuries by passive fluorescence and photochemical reflectance index, Intl. J. Remote Sens., 29, 5409–5422, 2008. 8284

Meroni, M., Rossini, M., Guanter, L., Alonso, L., Rascher, U., Colombo, R., and Moreno, J.: Remote sensing of solar-induced chlorophyll fluorescence: Review of methods and applications, Remote Sens. Environ., 113, 2037–2051, 2009. 8283, 8284, 8297

Meroni, M., Busetto, L., Colombo, R., Guanter, L., Moreno, J., and Verhoef, W.: Performance of spectral fitting methods for vegetation fluorescence quantification, Remote Sens. Env., 114, 363–374, 2010. 8289

Middleton, E. M., Corp, L. A., and Campbell, P. K. E.: Comparison of measurements and FluorMOD simulations for solar induced chlorophyll fluorescence and reflectance of a corn crop under nitrogen treatments, Intl. J. Rem. Sensing, Special Issue for the Second International Symposium on Recent Advances in Quantitative Remote Sensing (RAQRSII), 29, 5,193–5,213, 2008. 8284

Middleton, E. M., Cheng, Y.-B., Corp, L. A., Huemmrich, K. F., Campbell, P. K. E. Zhang, Q.-Y., Kustas, W. P. and Russ, A. L.: Diurnal and seasonal dynamics of canopy-level solar-induced chlorophyll fluorescence and spectral reflectance indices in a cornfield, Proc. 6th EARSeL SIG Workshop on Imaging Spectroscopy, CD-Rom, 12 pp., Tel-Aviv, Israel March 16-19, 2009. 8284

Moya I., Camenen, L. Evain, S. et al.: A new instrument for passive remote sensing : 1. Measurements of sunlight-induced chlorophyll fluorescence. Remote Sens. Environ., 91, 186–197, 2004. 8284

Myneni, R. B., Hoffman, W., Knyazikhin, Y., Privette, J. L., Glassy, J., Tian, Y., Wang, Y., Song, X., Zhang, Y., Smith, G. R., Lotsch, A., Friedl, M., Morisette, J. T., Votava, P., Nemani, R. R., and Running, S. W.: Global products of vegetation leaf area and fraction absorbed PAR from year one of MODIS data. Remote Sens. Environ., 83, 214–231, 2002. 8292

Nepstad, D. D., de Carvalho, C. R., Davidson, E. A., Jipp, P. H., Lefebvre, P. A., Negreiros, G. H., da Silva, E. D., Stone, T. A., Trumbore, S. E., and Vieira, S.: The role of deep roots in the hydrological and carbon cycles of Amazonian forests and pastures. Nature, 372, 666–669, 1994. 8295

Rascher, U.: FLEX – Fluorescence Explorer: A remote sensing approach to quatify spatio-temporal variations of photosynthetic efficiency from space, Photosynth. Res., 91, 293–294, 2007. 8297

Rascher, U., I. Agati, L. Alonso, et al.: CEFLES2: the remote sensing component to quantify photosynthetic efficiency from the leaf to the region by measuring sun-induced fluorescence in the oxygen absorption bands. Biogeosci., 6, 1181–1198, 2009. 8285

Rast, M. J., Bézy, J. L., and Bruzzi, S.: The ESA Medium Resolution Imaging Spectrometer MERIS - A review of the instrument and its mission. Int. J. Remote Sens., 20, 1681–1702, 1999. 8285

Reuter, M., Buchwitz, M., Schneising, O., Heymann, J., Bovensmann, H., and Burrows, J. P.: A method for improved SCIAMACHY CO_2 retrieval in the presence of optically thin clouds, Atmos. Meas. Tech., 3, 209–232, 2010. 8298

Rienecker, M. M., Suarez, M. J., Todling, R., et al.: The GEOS-5 data assimilation system - Documentation of versions 5.0.1, 5.1.0, and 5.2.0. NASA Tech. Memo. 2007-104606, vol. 27, M. J. Suarez, Editor., 2007. 8292

Rothman, L. S., Jacquemart, D., Barbe, A., et al.: The HITRAN 2004 molecular spectroscopic database, J. Quant. Spectrosc. Radiat. Trans., 96, 139–204, 2005. 8287

Sioris, C., Courrèges-Lacoste, G. B. and Stoll M. P.: Filling in of Fraunhofer lines by plant fluorescence: Simulations for a nadir-viewing satellite-borne instrument. Geophys. Res. Lett., 108, 4133, doi:10.1029/2001JD001321, 2003. 8289

van der Tol, C., Verhoef, W., and Rosema, A.: A model for chlorophyll fluorescence and photo-synthesis at leaf scale, Agricult. Forest Meteorol., 149, 96–105, 2009. 8283

Yokota, T., Yoshida, Y., Eguchi, N., Ota, Y., Tanaka, T., Watanabe, H., and Maksyutov, S.: Global Concentrations of CO_2 and CH_4 Retrieved from GOSAT: First Preliminary Results, Sci. Online Lett. Atm., 5, 160–163, 2009. 8286

Zarco-Tejada, P. J., Berni, J. A. J., Suarez, L., Sepulcre-Cantó, G., Morales, F., and Miller, J. R.: Imaging chlorophyll fluorescence with an airborne narrow-band multispectral camera for vegetation stress detection, Remote Sens. Environ., 113, 1262–1275, 2009. 8284

Title Page

Abstract | Introduction

Conclusions | References

Tables | Figures

◄ | ►

◄ | ►

Back | Close

Full Screen / Esc

Printer-friendly Version

Interactive Discussion
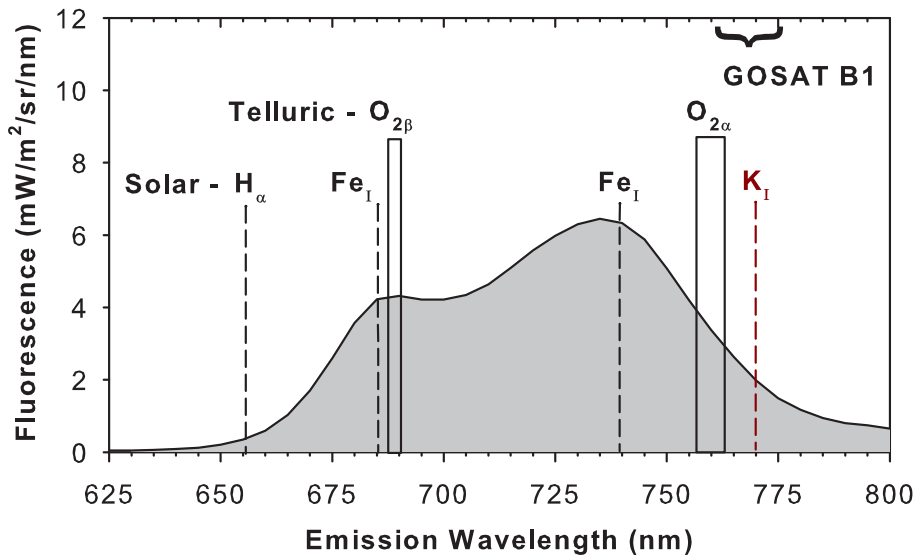
Fig. 1. Simulated solar-induced fluorescence as a function of the emission wavelength with locations of oxygen absorption bands and several solar Fraunhofer lines indicated including the K I line used here.
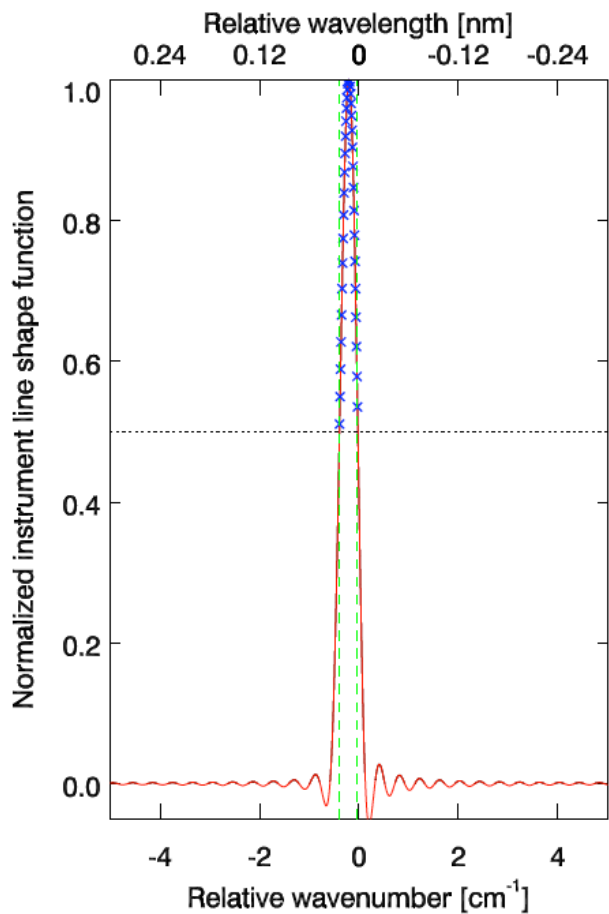
Fig. 2. GOSAT instrument line shape function with spectral sampling indicated in the full-width half-maximum portion.

Full Screen / Esc

Printer-friendly Version

Interactive Discussion
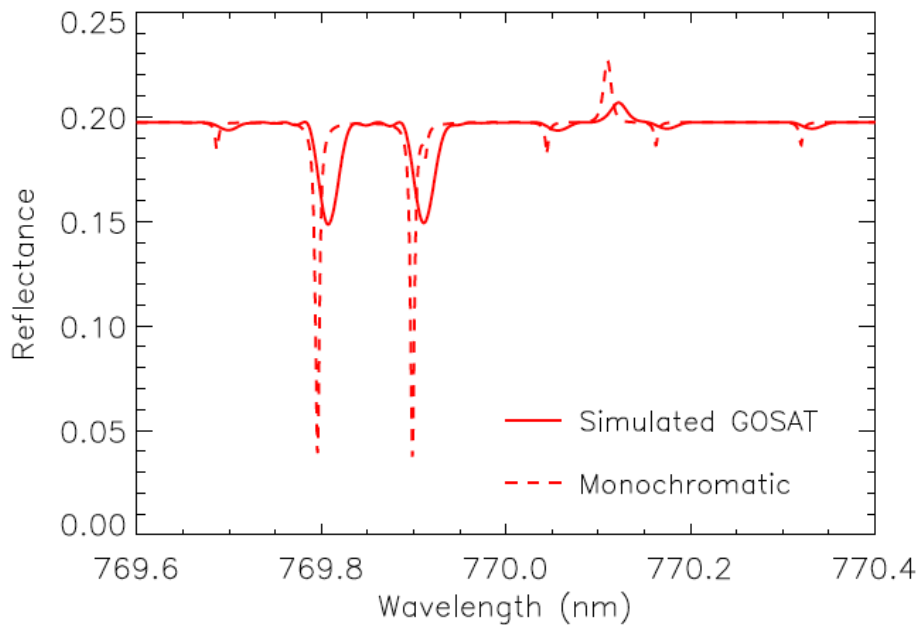
Fig. 3. Simulated monochromatic and GOSAT reflectance spectra assuming a fluorescence of $3\,\text{mW/m}^2/\text{sr/nm}$, SZA=45°, surface albedo=0.2.
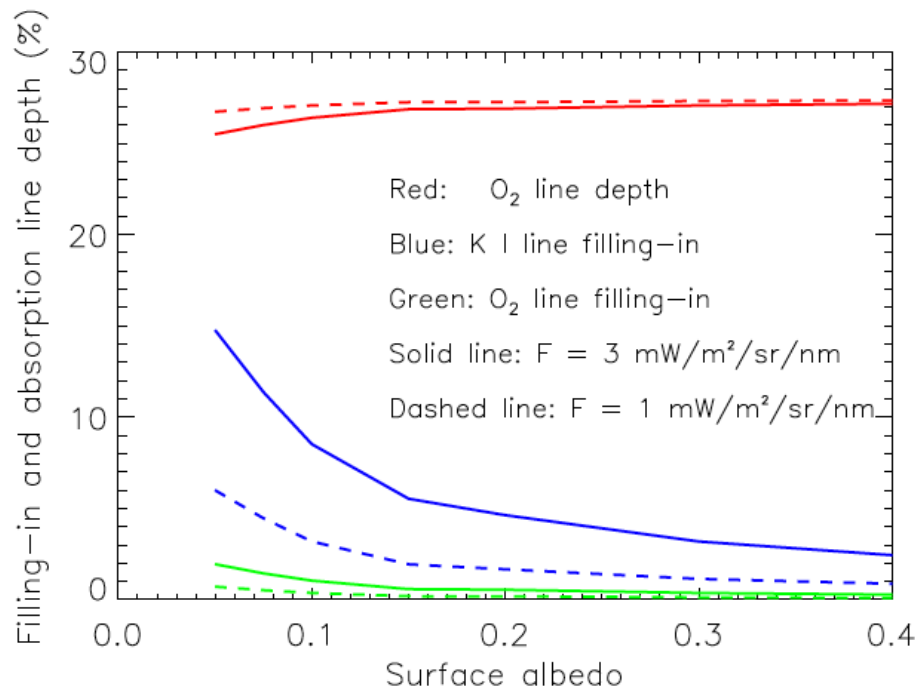
Fig. 4. Simulated GOSAT filling-in of and absorption from the O_2 weak line at 769.9 nm and filling-in of the K I line as a function of surface albedo.
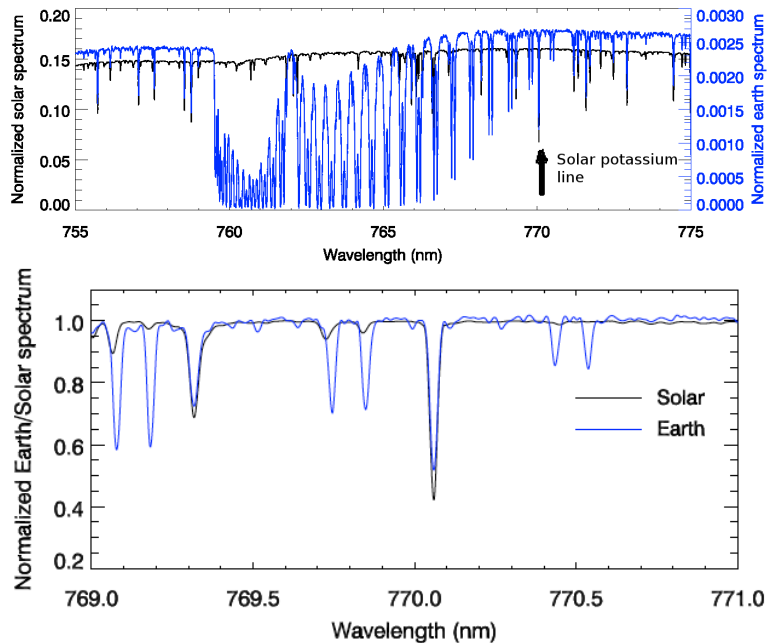
Fig. 5. GOSAT solar and Earth spectra in band 1 with the K I line (top) and zoom near the wavelengths used in our fitting window (bottom).
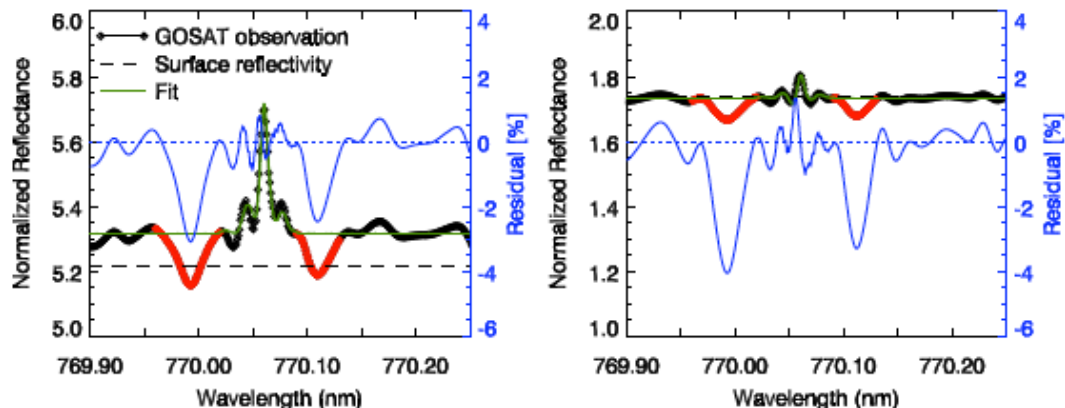
Fig. 6. Normalized reflectance (Earth radiance normalized by the solar spectra, black and red diamonds, left side axis), spectral fit (green solid line), derived reflectivity (black dashed line), and fit residuals (blue solid line, right side axis) in the vicinity of the K I Fraunhofer line showing contrast between active vegetation over the Eastern United States (left) and the Sahara (right) on 2 July and 1 July 2009, respectively. Note that the reflectance scales differ on these two panels.
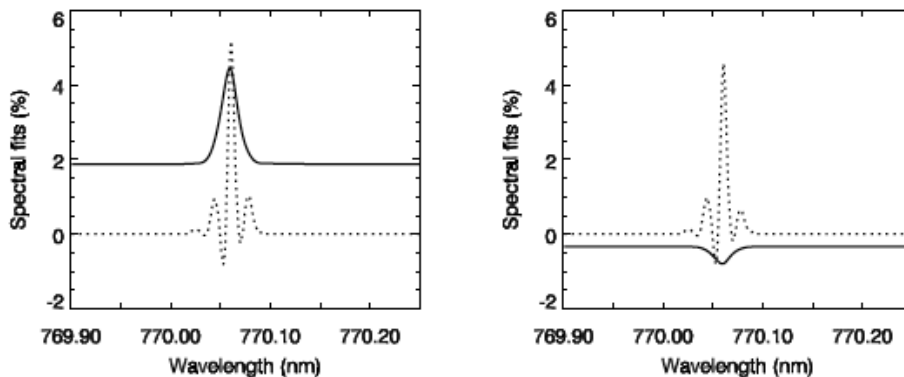
Fig. 7. Fitted unexplained (dotted) and fluorescence (solid) spectral structure as a percent of the continuum reflectance for the same two pixels shown in Fig. 6 (Eastern US on left and Sahara on right).
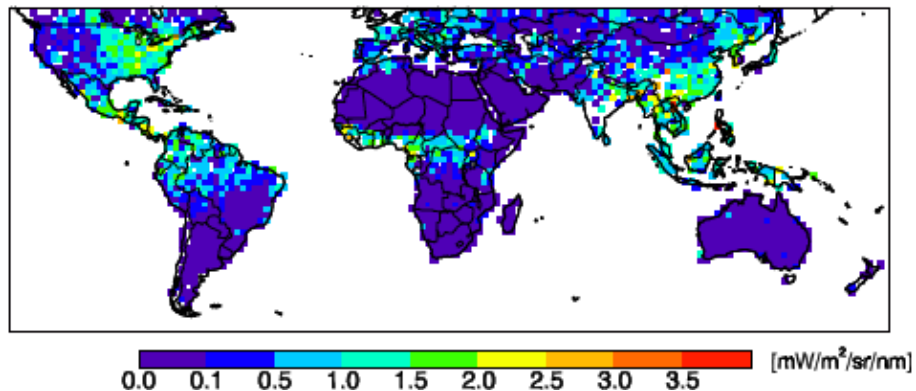
Fig. 8. Derived monthly averages for instantaneous fluorescence F (mW/m^2/sr/nm) from GOSAT for July 2009.
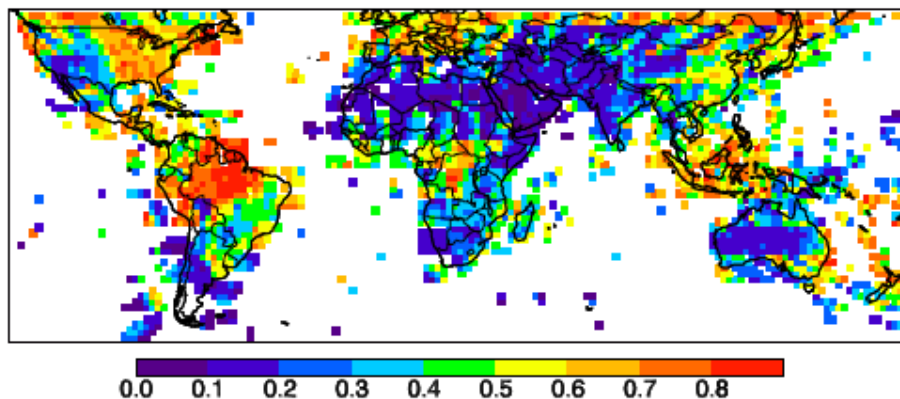
Fig. 9. 8-day FPAR product (unitless) from MODIS for 20–27 July 2009.

Full Screen / Esc

Printer-friendly Version

Interactive Discussion
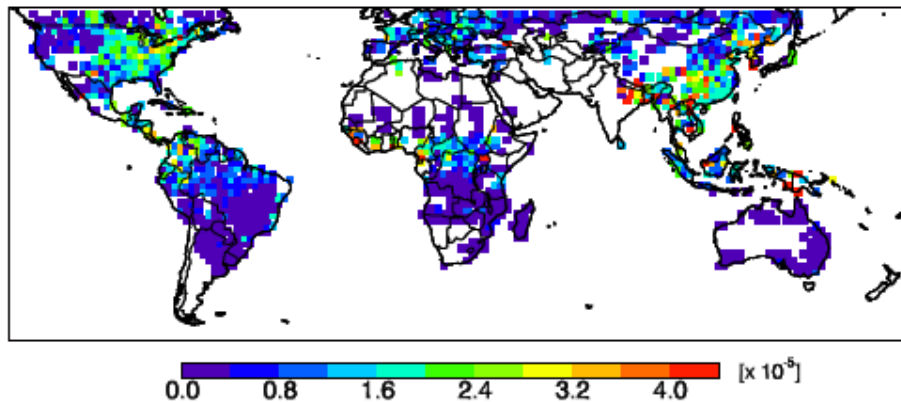
Fig. 10. Derived monthly averages for instantaneous fluorescence quantum yield, Φ, (unitless) for July 2009.
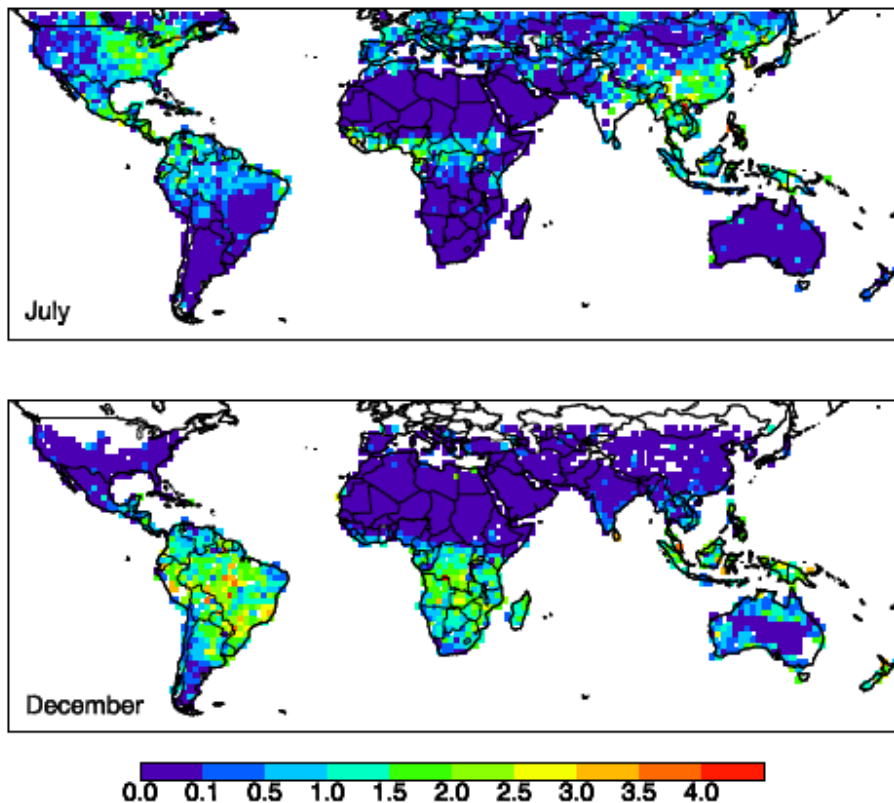
Fig. 11. Derived monthly averages for scaled fluorescence (unitless) from GOSAT for July and December 2009.
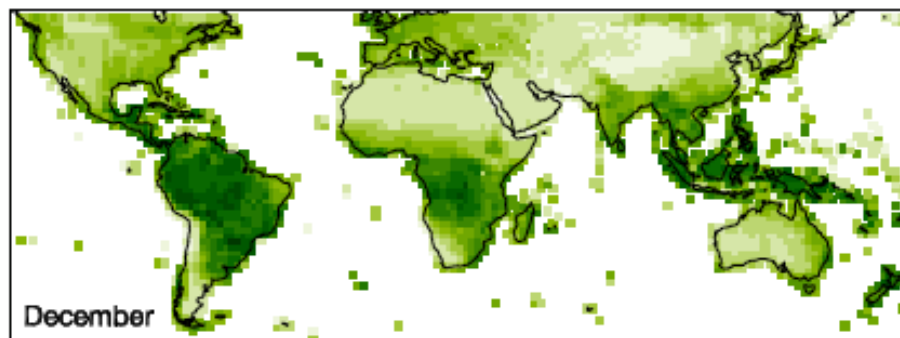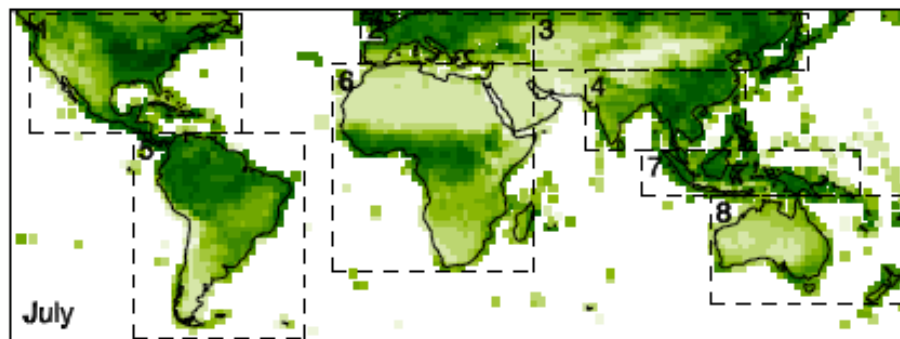
Fig. 12. Enhanced Vegetation Index (EVI) (unitless) from Aqua MODIS for July and December 2009. Boxes in top panel indicate regions of interest that will be further explored in Figs. 13–15.

Fig. 13. Scatter plots of the GOSAT scaled fluorescence versus the MODIS enhanced vegetation index (EVI) (both unitless) for July 2009 for different regions shown in Fig. 12. Each point represents a monthly mean from a single 2° × 2° grid box.
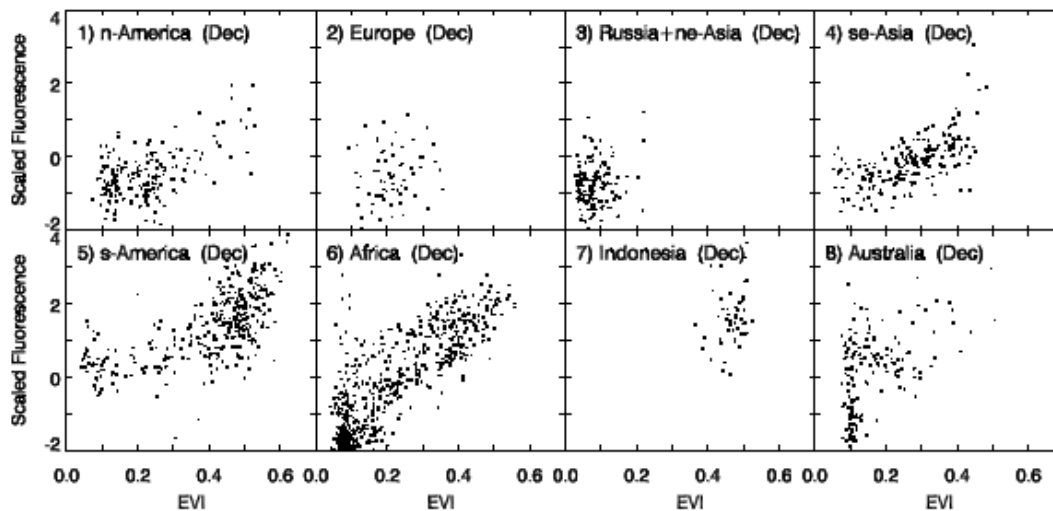
Fig. 14. Similar to Fig. 13 but showing scaled fluorescence versus the MODIS enhanced vegetation index (EVI) (both unitless) for December 2009.
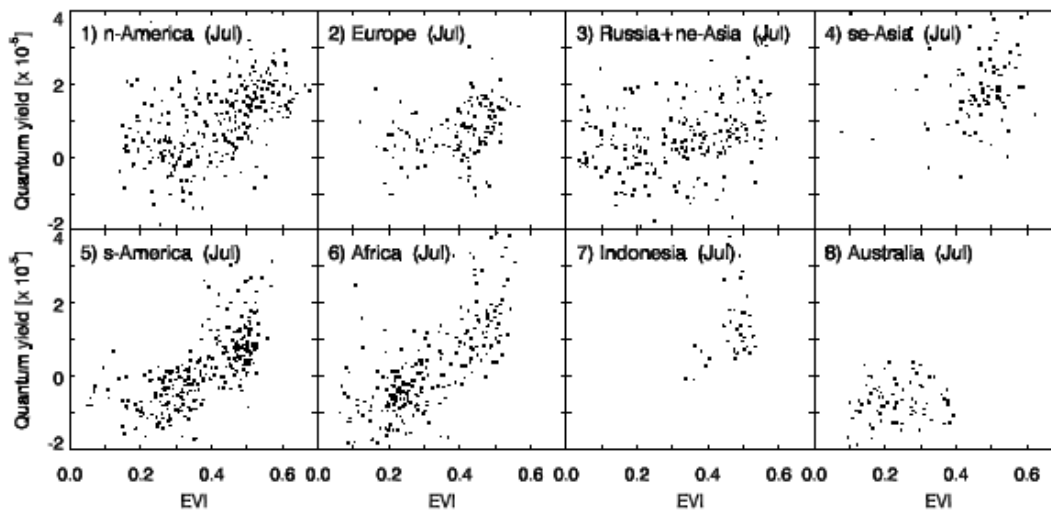
Fig. 15. Similar to Fig. 13 but showing derived fluorescence quantum yield, Φ, versus MODIS EVI (both unitless) for July 2009.
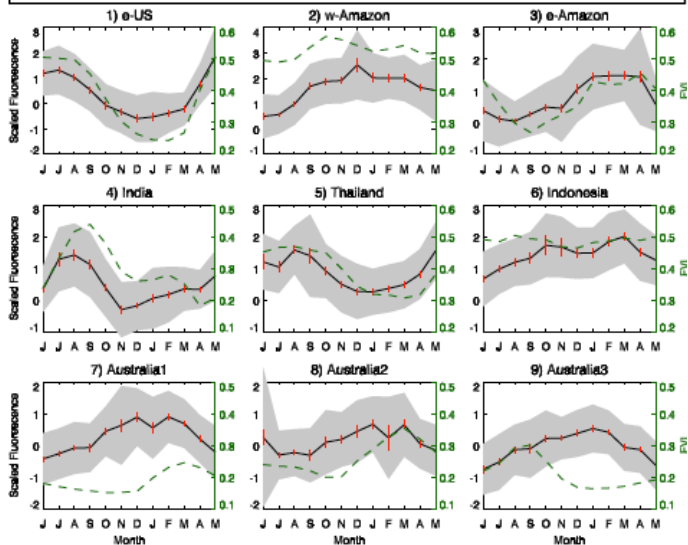
Fig. 16. Bottom panel: Full seasonal cycle in scaled *F* (left axis, unitless) for the regions indicated in the top panel; Black line: Monthly means; Red line: Errors of the mean; Shaded gray: standard deviation; Dashed green line: MODIS EVI (right panel, unitless).